Laser ablation of copper in different background gases: comparative study by numerical modeling and experiments

Annemie Bogaerts,* Zhaoyang Chen and Davide Bleiner

Received 10th October 2005, Accepted 30th January 2006
First published as an Advance Article on the web 17th February 2006
DOI: 10.1039/b514313f

A comprehensive model was developed to describe laser ablation of metals (Cu) with expansion in different background gases, *i.e.*, He, Ne, Ar, Kr and N_2. The effect of the background gas on the target heating, melting and vaporization, and on the plume expansion dynamics and plasma formation and plasma shielding, is investigated. It is found that the heavier background gases result in a slower expansion, or more confinement, of the vapour plume. Although background gases with a lower ionization potential exhibit a higher ionization degree in the plasma, this effect is of minor importance compared with the ionization of the vapour plume. Hence, the model predicts that the background gas has no significant influence on the plume temperature and electron density in the early stage of laser ablation (100 ns). Moreover, because laser absorption in the plasma mainly takes place in the vapour plume, plasma shielding is only slightly affected by the background gas. Nevertheless, the effect is large enough to yield some differences in the target evaporation depths, which are calculated to be slightly deeper for He than for Ne, Ar and Kr. These calculation results are in reasonable agreement with crater depths measured in the case of the different background gases.

1. Introduction

Laser ablation (LA) is a widely used sampling technique in analytical chemistry, for the analysis of solid materials. A laser is focused on the surface of the material to be analyzed, the so-called target material. This causes, among other things, heating and subsequent melting and vaporization of some of the material. The evaporated atoms of the target material form a plume, which expands, usually in a background gas (*i.e.*, the gas that fills the ablation cell, also called the "ambient gas"). Because the temperature in the expanding plume is very high (*i.e.*, typically a few 10 000 K), a plasma will be created, and this forms the basis of laser-induced breakdown spectroscopy (LIBS).[1–4] Indeed, the plasma consists of neutrals, ions and electrons, as well as excited species, and the latter emit characteristic photons when they decay to the ground state, which can be measured with optical emission spectrometry. On the other hand, the material plume will gradually cool down upon expansion, leading to the condensation of the vapour atoms, which results in the formation of nanometre sized particles of the material to be analyzed.[5] Besides, particles can also be ejected directly from the target material, *e.g.*, by mechanical fragmentation as a result of laser-induced stress[6] (such as for organic or geological materials), by splashing of the molten material,[5–7] or explosive boiling of the target.[8,9] All these particles, of nanometre and micrometre sizes, will form aerosols which can be transported from the laser ablation cell to an inductively coupled plasma (ICP), where they will be vaporized (*i.e.*, atomized) and subsequently ionized and/or excited, so that they can be measured with mass spectrometry or optical emission spectrometry (LA-ICP-MS and LA-ICP-OES).[10–15]

For good analytical practice of these techniques, a thorough insight in the processes taking place during and after laser ablation is desirable. For this purpose, we have developed a numerical model, which describes the laser-induced heating, melting and vaporization of the target material, followed by expansion of the evaporated plume and plasma formation, as well as the laser–plasma interaction. Initially, a model was developed for expansion in vacuum.[16,17] This model was subsequently extended to expansion in 1 atm He gas, which appeared to be much more complicated, due to the interaction between vapour and gas.[18,19] Indeed, there are several models available in the literature, describing laser ablation in vacuum (or low pressure, *i.e.*, up to 100 Pa) conditions. A complete overview can be found in ref. 17. However, there are only a few models presented in the literature for expansion in 1 atm background gas, and moreover these modelling approaches[20–24] often treat only the vapour species, or do not consider the interaction between vapour and background gas. In refs. 25–27, a hydrodynamic model, which describes the behavior of both vapor and background gas in a binary gas mixture, has been developed. However, it was applied to laser pulses in the ms-range, at very low laser irradiance (*i.e.*, 10^4–10^5 W cm^{-2}), so that plasma formation can be neglected. Recently, the same model was also applied to ns-laser pulses at a laser irradiance of 10^9 W cm^{-2}, which are typical conditions for LIBS and LA-ICP-MS/OES, but plasma formation was still not included,[28] although it is clear that a plasma is certainly created under such conditions. To our knowledge, there exist no models yet that describe the process of laser ablation with expansion in 1 atm background gas, including

University of Antwerp, Department of Chemistry, Universiteitsplein 1, B-2610 Wilrijk-Antwerp, Belgium.
E-mail: annemie.bogaerts@ua.ac.be

plasma formation, except for the model developed in our group.[18,19] It should, however, be mentioned that our model does not yet take into account any of the particle formation mechanisms described above, but this will be one of the next steps in the model development.

In a recent paper, we have applied our model to investigating the influence of laser parameters (*i.e.*, laser irradiance, pulse duration and wavelength) on the laser ablation, plume expansion and laser-induced plasma formation.[29] However, up to now the model was always focused on Cu as the target material, and He as the background gas. In the present paper we want to investigate numerically the effect of different background gases.

A number of papers have experimentally investigated the effect of background gas on the mass ablation rate, the plume temperature and the electron number density, and the analyte signal emission intensities in the laser-induced plasma or in the ICP. Russo and co-workers measured a higher amount of ablated mass,[30] and consequently a stronger ICP emission intensity,[30–32] in the order He > Ne > Ar > Kr > Xe, and this was explained by the higher ionization potential of He, yielding less plasma shielding.[30–32]

Iida[33] also observed an appreciable effect of the ambient atmosphere on sample vaporization, plasma emission intensity, excitation temperature and electron number density, in a comparison between He, Ar and air. Several differences were reported: there is more laser–plasma interaction in Ar than in He, yielding a higher electron number density in Ar, and consequently more plasma shielding, leading to a lower amount of vaporization in Ar. Also, the plume expansion rate was found to be higher in He than in Ar, due to its lower mass. Moreover, it was reported that the He plasma cools faster than the Ar or air plasma, due to the higher thermal diffusivity. Further, some differences observed between the Ar and air plasma were attributed to different specific heats and different degrees of freedom, associated with the possibility of vibrational excitation in the molecular gas.[33]

Niemax and collaborators[34] reported also that the crater diameter, depth and ablation rate drop in the order He > Ne > air > Ar. The measured emission intensity of the laser-induced plasma, on the other hand, was found to decrease in the order Ar > Ne > He, whereas the results for air were similar to the ones for He. This was attributed to the stronger plasma excitation in Ar, because of the higher plume temperature and electron density. Hence, in spite of the lower ablation in Ar, due to more plasma shielding, it was concluded that Ar gave the best results as background gas, at a reduced pressure, because of the higher plume temperature and hence more plasma emission. At atmospheric pressure, Ne might be a better choice, but a higher laser irradiance should then be applied.[34]

In ref. 35, He, Ar, Xe and air were compared as background gases, at pressures ranging from vacuum to 1 atm, for a Nd:YAG laser of 532 nm followed by a second (dye) laser for resonant excitation of the ablated material. The largest signal enhancement was observed in Xe at 13 mbar, despite the more severe plasma shielding and the lower etch rate.[35]

Jackson and Günther[36] compared the effect of He and Ar on the particle size distribution, for a Nd:YAG laser of 266 nm and an excimer laser of 193 nm, and pure Cu samples. They measured a larger fraction of small particles in He than in Ar.[36] In another paper, Horn, Guillong and Günther reported that measured ablation rates for various metals were not affected by a change in the ablation environment from Ar to He.[37]

In ref. 38, a comparison was made between He and air as background gases, for a Nd:YAG laser of 1064 nm and an Er:YAG laser of 2940 nm, and Al alloy samples, and it was found that He yields a lower electron number density than air because of the higher ionization potential. The electron number density was observed to be somewhat higher in He than in air, in the early times (at least for the Er:YAG laser), but it dropped more quickly due to the higher thermal conductivity of He.[38]

Finally, in ref. 39, Ar, air and N_2 were compared as the background gases for a Nd:YAG laser of 1064 nm, and Cu and Al targets. In the early stage, the ambient gas has no influence on the plume temperature, because the plasma is entirely composed of metal vapour and it repels the ambient gas by the snowplough effect. After a few tens of ns, a mixed plasma begins to develop in the vicinity of the metal plasma, and after some hundreds of ns, the ambient gas reaches the core of the metal plasma by diffusion. At the beginning of mixing, a higher plume temperature was observed in Ar than in air, because in air the energy is also used for dissociation, besides ionization, meaning an additional energy loss channel.[39]

Hence, it is clear that the background gases have some effect on the mass ablation rate, expansion dynamics and plasma behavior. To investigate this effect in more detail, and quantitatively, the present paper reports the results of our numerical model applied to laser ablation of a Cu target, with expansion in different background gases, including He, Ne, Ar, Kr and N_2. Moreover, comparison will be made with experimental results for the crater depth obtained by LA in these gases.

2. Description of the model

As was mentioned above, the model describes several aspects of laser ablation, including:

(a) laser–solid interaction: heating, melting and vaporization of the Cu target;

(b) plume expansion in 1 atm background gas;

(c) plasma formation and laser–plasma interaction, leading to so-called plasma shielding.

We will not go into detail about the model, because it was explained thoroughly in refs. 18 and 19, but we will briefly point out the main aspects.

The target heating, *i.e.*, the temperature distribution inside the target material, is calculated with a one-dimensional heat conduction equation. When the temperature reaches the melting point, melting of the solid material will take place, but the same heat conduction is still used, albeit with other thermal properties (*i.e.*, for the molten phase). At still higher temperature, vaporization can become important, and the resulting calculated vapor density, velocity and temperature at the target serve as boundary conditions for the second part of the model. Note that other processes at the target, such as explosive boiling and splashing of the melt, are not yet taken into account.

The vapor plume expansion in 1 atm background gas, including the interaction between vapour and gas, is described with Navier–Stokes equations for conservation of total mass density, vapor mass density, momentum and energy in a binary gas mixture. Further, because of the high temperature in the plume, the vapour and background gas become ionized, and a plasma is created consisting of ions and electrons, beside neutral atoms. For the background gases, only singly charged ions are taken into account, whereas for the target materials, which generally have a lower ionization potential (see below), doubly charged ions are also considered. Since the plasma can be considered in local thermal equilibrium, the first (and second) order ionization degrees of metal and gas are calculated from the plume temperature, with Saha–Eggert equations. Finally, the laser beam will also interact with the created plasma, and it will partially be absorbed before reaching the target. The absorption mechanisms taken into account are electron–neutral and electron–ion inverse Bremsstrahlung (e–n IB, e–i IB), as well as photoionization (PI) from excited levels (see refs. 18 and 19 for more explanation).

It is important to realize that the target evaporation determines the vapour plume expansion dynamics, and *vice versa*, the vapour influences the target boundary conditions. Further, the laser beam absorption in the plasma affects the target (since it reduces the effective laser irradiance reaching the target) and it also causes heating of the plasma. Therefore, the various parts of the model are strongly coupled, and need to be solved simultaneously as a function of time, in order to obtain an overall picture of laser ablation, plume expansion and plasma formation. The details of the model, *i.e.*, equations used, boundary conditions, coupling of the different parts, and solution procedure, can be found in ref. 19.

3. Experimental setup

The measurements were performed with a laser micro-sampler Nd:YAG (Quanta-Ray DCR-11, Spectra-Physics) that was in-house modified. The frequency-quadrupled wavelength (266 nm, Q-switched with 6 ns pulse length) was pulsed at 10 Hz, and a fluence of 17 J cm^{-2} for a 170 μm spot size was obtained using a 40-mm focal distance objective lens. The maximum laser irradiance corresponded to 2.9 GW cm^{-2}. The ablation cell was a 30 cm^3 cylindrical cell, provided with a 0.5 mm id inlet nozzle to ensure a steady gas inlet. Different ambient gases were used, namely Ar, He, N_2, air, Kr, and SF_6 at atmospheric pressure.

Profilometry measurements were carried out to determine the ablated depth and crater morphology. Five traces across the crater were acquired using a Tencor P-10 profilometer (KLA-Tencor, USA), with a stylus force of 5.0 mg, and moving speed of 20 μm s^{-1}, over a distance of 500 μm across the crater.

4. Results and discussion

The results presented in this paper are obtained from calculations for a Nd:YAG laser of 266 nm. The laser pulse has a Gaussian time-profile with 5 ns pulse duration (fwhm). Most calculations were performed for a laser irradiance of 1 GW cm^{-2}, unless mentioned otherwise. Calculations are always carried out up to 100 ns, because the model is one-dimensional, hence it assumes forward expansion of the vapour plume, and this is only a reasonable assumption up to an expansion distance in the order of 1 mm (depending on the laser spot size),[25,39–41] which corresponds typically to a time in the order of 100 ns. At later times, spherical expansion will become important, and this cannot yet be described with our model in its present stage.

4.1. Target heating, melting and vaporization

As mentioned above, the laser impact on the sample results in heating of the sample material, which causes melting and vaporization of the target material. The calculated temperature distribution inside the target as a function of time was presented in previous papers,[17–19,29] for vacuum and for He as the background gas, and will not be shown here again because the results look very similar for the different background gases. However, Fig. 1 illustrates the calculated surface temperature and evaporation depth at the Cu target as a function of time, for the different background gases. The surface temperature (Fig. 1(a)) rises as a result of the laser (photon) impact, up to a maximum of about 7000 K at 8 ns, which corresponds to the maximum of the laser irradiance time-profile (see schematic representation by the broken line in Fig. 1(a), in arbitrary units). As soon as the laser pulse is finished, the surface temperature drops quickly until about 3000 K after 20 ns, and then more slowly to about 1100 K at 100 ns. It is clear from Fig. 1(a) that the calculated surface temperature curves coincide for all different background gases investigated (He, Ne, Ar, Kr and N_2). The maximum surface temperature was calculated to be 7088 K for He, 7062 K for Ne, 7036 K for Ar, 7025 K for Kr, and 7037 K for N_2. Hence, it rises slightly with decreasing mass and increasing ionization potential of the background gas (see values given in Table 1), for the reason explained below, but the effect is almost negligible.

The influence of the background gas is somewhat more pronounced for the calculated evaporation depth, as is illustrated in Fig. 1(b). The evaporation depth increases dramatically after about 5 ns, when the surface temperature is sufficiently high to cause evaporation. It reaches a maximum at about 13–14 ns, and then drops slightly again, when recondensation starts to occur. The evaporation depth at 100 ns is calculated to be about 41 nm for He, 39 nm for Ne, 36 nm for Ar, 32 nm for Kr and 38 nm for N_2. At later times, *i.e.*, after steady-state has been be reached, the differences will become slightly larger, as can be seen from the trends in the curves, visible in Fig. 1(b). Hence, the minor differences in the calculated surface temperatures still have a visible effect on the evaporation depths, because the evaporation flux is a strong function of the surface temperature in this temperature range. In analogy to the surface temperature, the evaporation depth drops with increasing mass and decreasing ionization potential of the background gas. This is attributed to a somewhat higher amount of plasma shielding, so that less laser energy can reach the target, as will be explained later in this paper.

The same trend was also observed in some experiments, for the amount of ablated mass or crater depth,[30,33,34] although

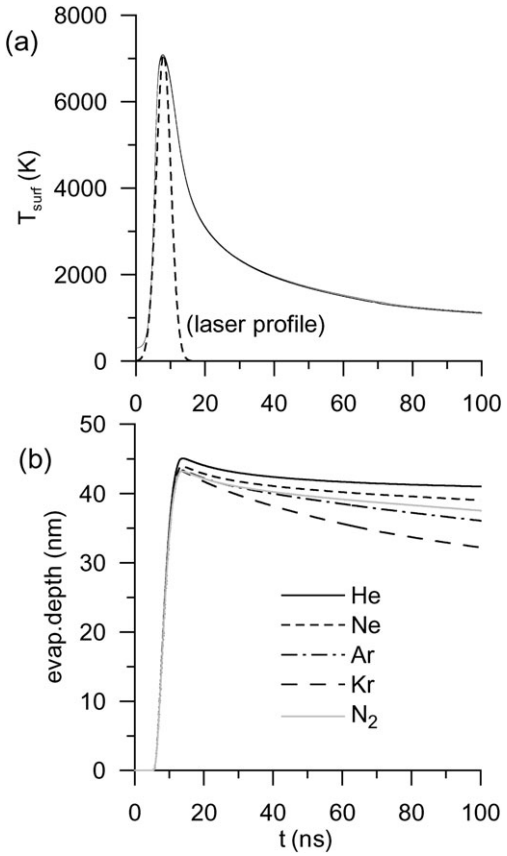

Fig. 1 Calculated surface temperature (a) and evaporation depth at the target (b), as a function of time, for the five different background gases (He, Ne, Ar, Kr and N_2), for a laser of 266 nm, with 5 ns FWHM, and an irradiance of 1 GW cm^{-2}. The laser irradiance–time profile is schematically illustrated (in arbitrary numbers) with the broken line in Fig. 1(a).

the effect was sometimes more pronounced than in our calculations, whereas in other experiments no clear difference was obtained.[37] Therefore, as mentioned above, we have also measured crater profiles for laser ablation in He, Ar, Kr, N_2 and air, and the results are shown in Fig. 2. This figure shows the depths obtained after 200 laser pulses, for a laser irradiance of 2.9 GW cm^{-2} (see Section 3 above). The profiles are far from being flat, which is attributed to an irregular laser beam profile. Possibly also other effects than vaporization, such as liquid splashing, phase explosion or back-condensation, play a role. A SEM picture of the crater obtained with Ar as the background gas (see Fig. 3) confirms this irregular crater shape, and also illustrates the occurrence of liquid splashing in the radial direction.

Therefore, the deepest point of the crater, measured relative to the original position of the surface, gives probably the best representation of the real crater depth at the laser irradiance of

Table 1 Mass and ionization potential of the different background gases investigated in this paper

Gas	He	Ne	Ar	Kr	N_2
Mass/amu	4.003	20.18	39.95	83.8	28.01
Ionization potential/eV	24.58	21.56	15.76	14.00	15.58

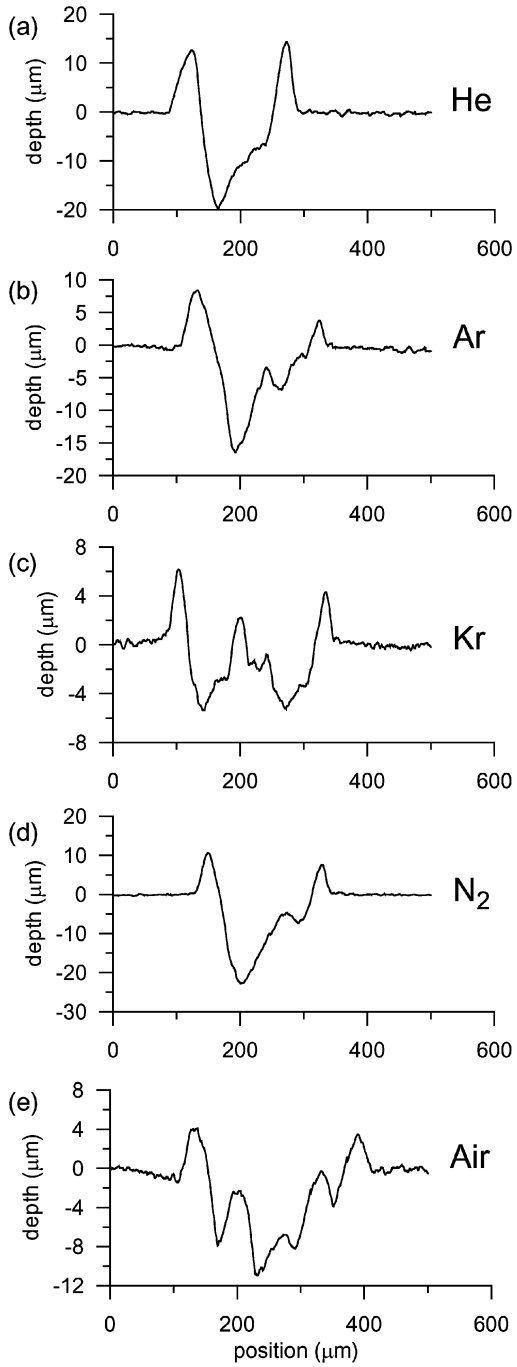

Fig. 2 Measured crater profiles after 200 laser pulses, for laser ablation in He (a), Ar (b), Kr (c), N_2 (d) and air (e), for a laser of 266 nm, with 6 ns FWHM, and an irradiance of 2.9 GW cm^{-2}.

2.9 GW cm^{-2}. If we divide this value by 200 laser pulses, we obtain the following crater depths per laser pulse for the different gases: 100 nm for He, 80 nm for Ar, 30 nm for Kr, 110 nm for N_2 and 60 nm for air. These values are typically a factor of 2 higher than our calculated values (see above). However, the experimental laser irradiance is also a factor of 3 higher, and in our previous paper[29] we predicted a rise in crater depth from *ca.* 40 nm at 1 GW cm^{-2} to *ca.* 100 nm at 3 GW cm^{-2} in the case of He (see Fig. 2 of ref. 29). Hence, this shows that the evaporation depths predicted by our model

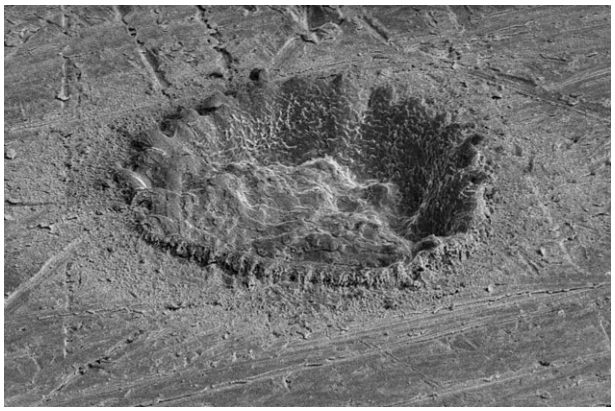

Fig. 3 Measured SEM picture of a typical crater obtained after 200 laser pulses, for laser ablation in Ar, for the same laser conditions as in Fig. 2.

yield realistic values for the crater depths, and it suggests that evaporation is the main mechanism of target ablation for the conditions under investigation, *i.e.*, relatively low laser irradiance of 1 GW cm^{-2}. Furthermore, the measured crater depth in He is somewhat larger than in Ar, and clearly larger than in Kr, whereas the crater depth in N_2 is comparable to the values in He and Ar. These trends are qualitatively very similar to our model predictions, although the measured difference between Ar and Kr is clearly larger than the calculated difference. However, this might also be an artifact in the measurements. The measured crater profile in Kr has, indeed, a very irregular shape. Finally, by comparing Figs. 2 (d) and (e), it is clear that the measured crater profile in N_2 is much deeper than in air. This suggests that the effect of O_2 in the air is quite pronounced. Indeed, O_2 is a much more reactive gas, which can lead to other laser energy absorption mechanisms in the plume/plasma, *i.e.*, not only dissociation of the molecules, but also chemical reactions of the reactive species. We observed a similar behaviour for laser ablation in SF_6 gas, where almost no ablation took place because of extremely high plasma screening. These chemical effects cannot yet be described with our model in its present stage, so that we limit ourselves to a comparison of the inert gases and N_2. In general, the observed trends in the measured crater profiles are similar to the calculated trends, which shows that our model presents a realistic picture of laser ablation, as well as plume expansion, plasma formation and plasma shielding, at least for the short time-scale up to 100 ns.

4.2. Plume expansion and plasma formation

When the Cu evaporates from the surface, a Cu vapour plume is formed in front of the target, which will expand and push the background gas away from the surface. This is visualized in Fig. 4, which illustrates the calculated density profiles of Cu vapour (broken lines) and He or Ar background gas (left and right set of figures, respectively; continuous lines), at different times. At short times (*e.g.*, 10 ns), the Cu vapour is at a maximum near the target, as a result of the vaporization. At later times, beyond 10 ns, vaporization has ceased, and the Cu vapour expansion is clearly seen, as well as its effect on the background gas, which is piled up in front of the vapor plume front. Note that the undisturbed background gas density is at 1 atm, which corresponds to a number density of 2.4×10^{25} m^{-3}. A clear difference is observed between the expansion dynamics in He and in Ar. Indeed, because of its larger mass, the Ar gas is able to confine the Cu vapour to a smaller volume, as appears from the differences in x-axes in the left and right set of figures. For instance, after 100 ns, the Cu vapour plume extends up to about 0.9 mm from the target in the case of expansion in He gas, and only up to about 0.4 mm in the case of expansion in Ar gas. Also, the background gas density profiles look different. Indeed, the He gas shows a broader maximum, whereas the Ar gas density increases steadily until a sharp maximum is reached at the shock front position, which is also clearly higher than in the case of He. This is again attributed to the larger mass of Ar, giving it more resistance against the "piston" effect of the Cu vapour. The overlap region between Cu vapour and background gas appears to be slightly larger in the case of Ar, which means that there is a bit more interaction (due to diffusion, viscosity and thermal conductivity) between the vapour and the background gas. It should, however, be mentioned that the Godunov scheme,[42] which is used for solving the Navier–Stokes equations, also introduces some mixing layer. This appears to be a numerical artifact, but we were not able to use another solution method because other methods, with higher order accuracy, were found to be unsuitable for describing the plasma formation in a stable way. However, we have tried to limit this numerical inaccuracy as much as possible, by using a very small spatial grid (which is at the expense of calculation time, of course). Typically, the calculations take about four days for laser ablation and expansion during 100 ns at the typical conditions investigated (1 GW cm^{-2}). By going to a higher laser irradiance the calculation time rises drastically; for instance, at 10 GW cm^{-2}, it becomes of the order of 10 days.

The density profiles of Cu vapour and (He or Ar) background gas are also plotted at different times in Fig. 5 (a) and (b), respectively. Fig. 5(c) shows the calculated plume velocities at these different times. Again, it is clear that the plume can expand much faster in He than in Ar. Indeed, the plume velocity is calculated to be of the order of 10 km s^{-1} for expansion in He, and only about 4–7 km s^{-1} in the case of expansion in Ar. The plume velocity also decreases more quickly with time for expansion in Ar, due to the more severe resistance of the Ar gas.

The calculated plume temperatures at different times, and for expansion in either He or Ar gas, are plotted in Fig. 5(d). The absolute values of the temperature in both cases are very similar, *i.e.*, around 50 000 K at 10 ns, and slightly decreasing until about 30 000 K at 100 ns. This result seems to be in contrast to observations in literature,[33,34] where a higher plume temperature was reported in Ar than in He. This was explained by the lower ionization potential of Ar, yielding more ionization and hence laser heating by inverse Bremsstrahlung, as well as by the higher thermal conductivity of He, yielding a faster cooling rate than in Ar.[33,34] However, the different plume temperature was only observed at a later stage of plasma emission, whereas our results are plotted for the first 100 ns of laser ablation, when the effect of a faster cooling rate

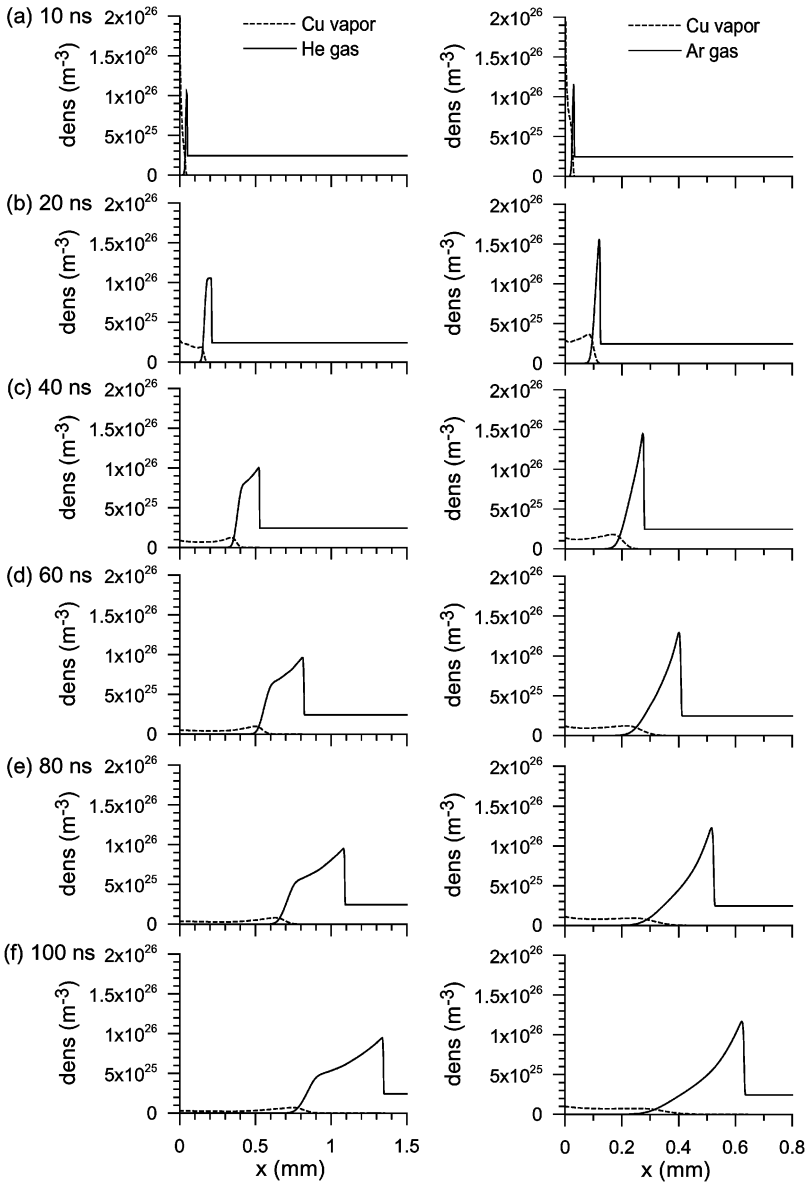

Fig. 4 Calculated density profiles of Cu vapor and background gas, at different times (10, 20, 40, 60, 80 and 100 ns), for the case of expansion in He (left set of figures) and Ar (right set of figures), for the same laser conditions as in Fig. 1.

is probably not yet significant and when the mixing between the Cu vapour and the background gas is not yet appreciable.

From Fig. 5(d) it is, however, clear that the temperature profiles for plume expansion in He and Ar look slightly different. Indeed, in the case of expansion in He, the plume temperature reaches a maximum near the maximum of the Cu vapour density (*cf*. Fig. 5(a)), and it drops clearly to lower values where the He gas is piled up. In the case of expansion in Ar, the plume temperature has its maximum also near the maximum Cu vapor density, but it does not show such a pronounced drop after the vapor plume front. The reason is that Ar has a lower ionization potential than He, yielding a higher ionization fraction in the Ar background gas, and hence more heating due to laser absorption in the background gas, as a result of inverse Bremsstrahlung (see below). Hence, this result is at least qualitatively in agreement with the experimental observations[34] (see above).

The calculations were also performed for expansion in Ne, Kr and N_2, and the results look qualitatively very similar, and follow the trends dictated by mass and ionization potential of the background gas (see Table 1), *i.e*., the plume expansion becomes slower in a heavier background gas (He > Ne > Ar > Kr), and the gas temperature shows a more pronounced drop after the vapour plume front for the gases with highest ionization potential (He > Ne > Ar > Kr). The results for expansion in N_2 were found to be similar to the results in Ar, because of the similar values of mass and ionization potential (*cf*. Table 1).

The calculation results for the different gases, at a time of 100 ns after the start of the laser pulse, are summarized in Fig. 6. The maximum Cu vapour density (a) appears to be slightly higher for expansion in the heavier background gases, because of the more severe confinement, but the effect is quite small. Also the background gas density (b) is slightly higher for the

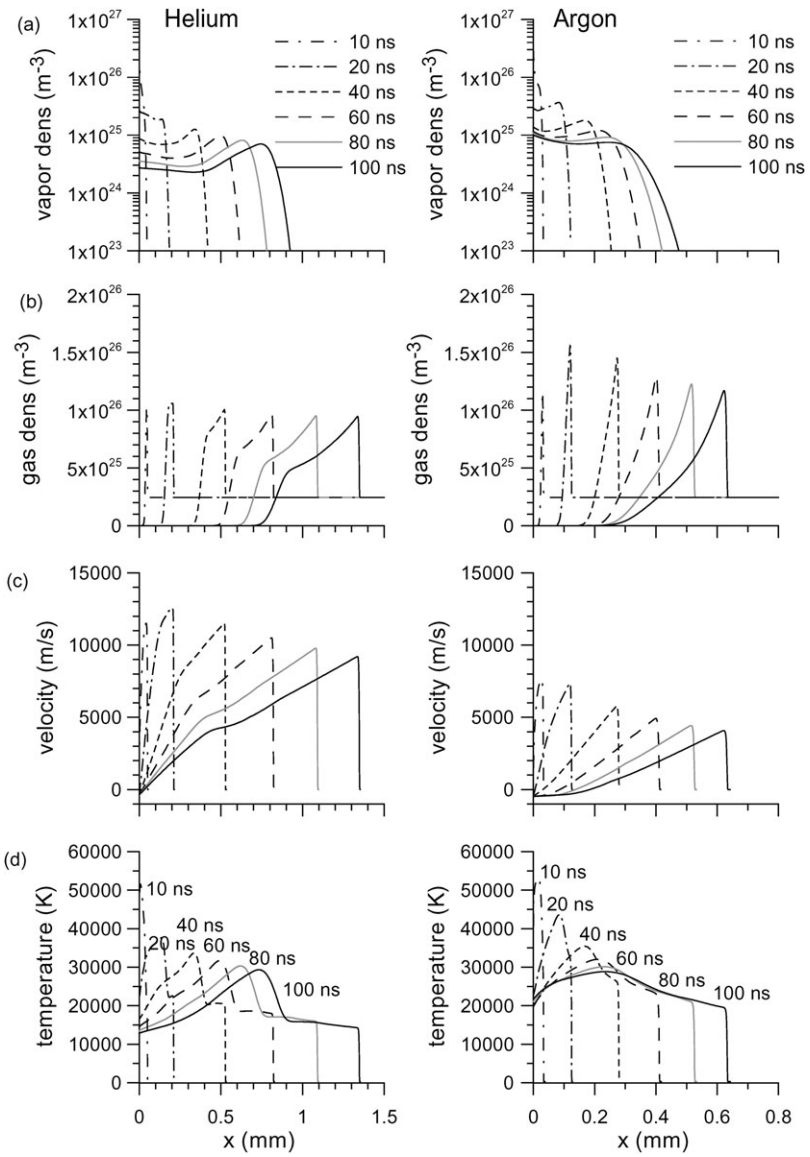

Fig. 5 Calculated density profiles of Cu vapor (a) and background gas (b), plume velocity distributions (c) and temperature profiles (d), at different times, for the case of expansion in He (left set of figures) and Ar (right set of figures), for the same laser conditions as in Fig. 1.

heavier gases, as was already apparent from Fig. 4. The plume velocity (c) drops drastically for expansion in a heavier gas, due to the more severe confinement and, as a result, the vapor plume (d) will be shorter and the shock front position (e), *i.e.*, the position where the piled-up background gas will return to its undisturbed value, will not reach such long distances. The maximum plume temperature (f) appears to be unaffected by the background gas, although it was clear from Fig. 5(d) that the shape will be somewhat different, because the temperature will not drop so drastically in a background gas with lower ionization potential. As a result of the similar values of maximum plume temperature, the ionization degree of Cu was calculated to be very similar for expansion in the different gases. It appears that most of the Cu in the plume is ionized, and the fractions of Cu^+ and Cu^{2+} ions were calculated to be about 0.7 and 0.3, respectively, for all different gases, at least at the position where the plume temperature was at its maximum. Closer to the target, the ionization degree was lower. The ionization degree of the background gas is illustrated in Fig. 6(h). The continuous and broken lines represent the fraction of neutral atoms (X^0) and ions (X^+) at the position of the maximum temperature, respectively. It is clear that the ionization degree of the background gas increases significantly with decreasing ionization potential, as expected. It should, however, be noted that this position of maximum temperature more or less coincides with the maximum in the vapour density, but that the background gas density here is very low (*cf.* Fig. 5). Hence, these curves do not really represent the overall ionization degree of the background gas. Therefore, the dash–dotted curve in Fig. 6(h) shows the ionization degree of the background gas at the position of its maximum density, *i.e.*, at the shock front position, where the plume temperature is much lower. It is logical that the ionization degree will then be much lower (up to 10% at maximum, for the conditions investigated). Consequently, as will be shown below, the background gas gives only a minor contribution to the total electron density in the plume. For this

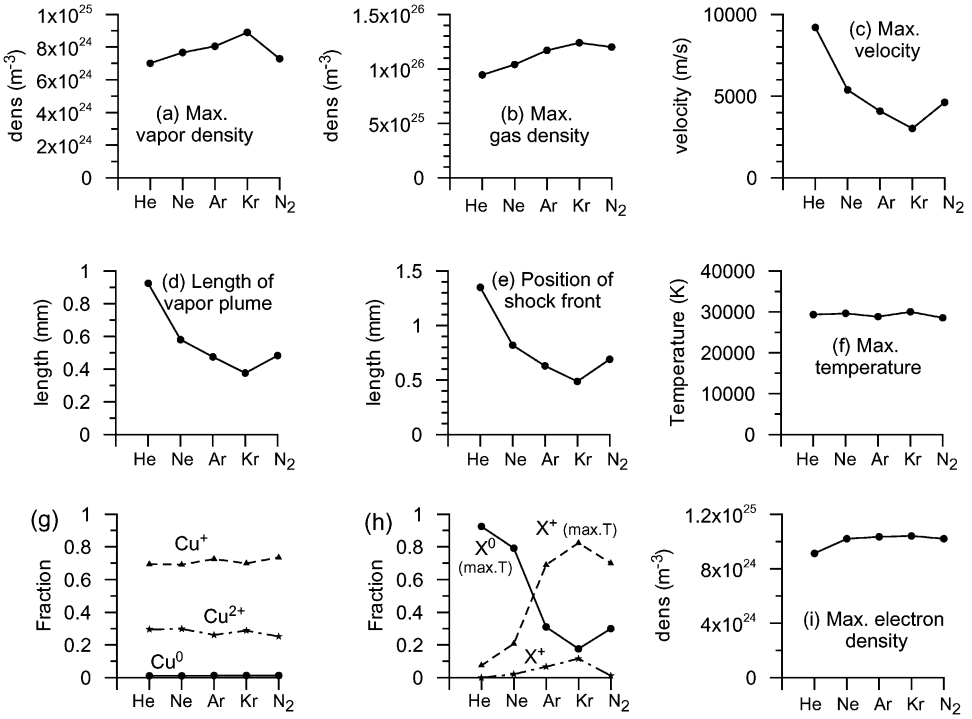

Fig. 6 Calculated maximum vapour number density (a), maximum background gas number density (b), maximum plume velocity (c), length of the vapour plume (d), shock front position (e), maximum plume temperature (f), fraction of Cu^0 atoms, Cu^+ and Cu^{2+} ions (g), fraction of gas atoms (X^0) and ions (X^+) (h), and maximum electron number density in the plume (i), at 100 ns, for expansion in different gases, for the same laser conditions as in Fig. 1.

reason, the maximum electron density at 100 ns is nearly unaffected by the background gas, as appears from Fig. 6(i).

4.3. Laser absorption in the plasma

As was mentioned in the introduction, several experimental research papers have already reported on the effect of the background gas on laser absorption in the plasma and plasma shielding. To investigate this effect in more detail, Fig. 7 (left set of figures) shows the calculated laser absorption coefficients as a function of position in the plume, at 8 ns, *i.e.*, at the maximum of the laser profile, for the different background gases, and for the three different laser absorption mechanisms taken into account in the model, *i.e.*, inverse Bremsstrahlung (IB) due to electron–neutral and electron–ion interactions (e–n IB and e–i IB) and photo-ionization (PI). IB involves the absorption of a (laser) photon by a free electron, so that the electron is raised to a higher state in the continuum. This process must occur within the field of a heavy particle (*i.e.*, an ion or neutral), to satisfy conservation of momentum. The e–n IB and e–i IB absorption coefficients are calculated as:

$$\alpha_{\mathrm{IB,e\text{-}n}} = \left[1 - \exp\left(-\frac{hc}{\lambda kT}\right)\right] N_{\mathrm{e}} \left(Q_{\mathrm{e-Cu}} N_{\mathrm{Cu^0}} + Q_{\mathrm{e-X}} N_{\mathrm{X^0}}\right)$$

$$\alpha_{\mathrm{IB,e\text{-}i}} = \left[1 - \exp\left(-\frac{hc}{\lambda kT}\right)\right] \frac{4e^6 \lambda^3 N_{\mathrm{e}}}{3hc^4 m_{\mathrm{e}}} \left(\frac{2\pi}{3 m_{\mathrm{e}} kT}\right)^{1/2} \times \left(N_{\mathrm{Cu^+}} + 4N_{\mathrm{Cu^{2+}}} + N_{\mathrm{X^+}}\right)$$

where λ is the laser wavelength, N_{e} is the electron number density, T is the plume temperature, $N_{\mathrm{Cu^0}}$, $N_{\mathrm{Cu^+}}$, $N_{\mathrm{X^{2+}}}$, $N_{\mathrm{X^0}}$ and $N_{\mathrm{X^+}}$ represent the Cu^0, Cu^+, Cu^{2+}, gas atom (X^0) and ion (X^+) number densities, respectively, Q is the cross section of photon absorption (assumed to be 10^{-46} m^5 for Cu, and 10^{-48} m^5 for the background gases, as derived from ref. 43), and the other symbols are self-explanatory.

The third absorption mechanism is photo-ionization of excited atoms. Atoms in excited levels are not yet explicitly included in our model, but we calculate their relative population, based on the Boltzmann distribution of statistical thermodynamics theory:

$$p_i = \frac{N_i}{N_{\mathrm{tot}}} = \frac{g_i \exp(-E_i/kT)}{\sum_j g_j \exp(-E_j/kT)}$$

where p_i and N_i stand for the relative and absolute population density of level i, N_{tot} is the total population density of all levels, g_i and E_i represent the statistical weight and excitation energy of level i, and T is the plasma temperature. The PI absorption coefficient is approximated as $\sigma_{\mathrm{PI,Cu}} N_{\mathrm{Cu}}$ where N_{Cu} is the Cu vapour number density, and σ_{PI} is the cross section of photo-ionization, estimated based on a constant value of 1.5×10^{-21} m^2, as found in the literature,[44,45] but corrected for the availability of excited levels lying close enough to the ionization limit (based on the relative populations as calculated above), so that the energy difference is smaller than the energy of the laser photons. Note that photo-ionization was neglected for the background gases, because of their much higher ionization potential.

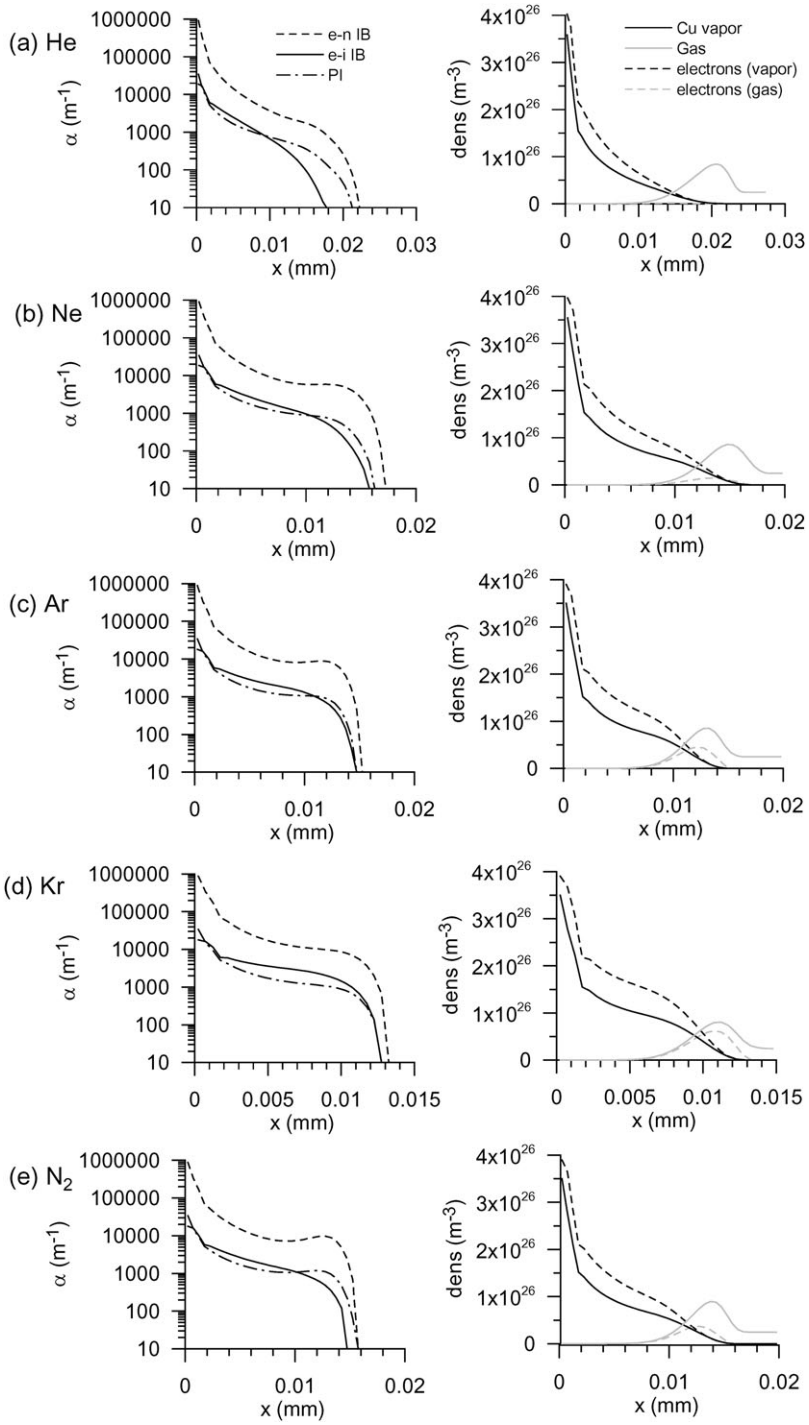

Fig. 7 Calculated absorption coefficients of e–n IB, e–i IB and PI (left set of figures), and calculated densities of Cu vapour, background gas and electrons originating from Cu vapour and background gas, respectively (right set of figures), as a function of position in the plume, at 8 ns, for expansion in different gases, for the same laser conditions as in Fig. 1.

As appears from Fig. 7 (left set of figures), e–n IB appears to be the dominant laser absorption mechanism throughout the entire plume, for all the gases investigated, whereas e–i IB and PI seem to play a similar, but less important role. Furthermore, it is clear that the laser absorption mainly takes place near the target, *i.e.*, in the vapour plume. Indeed, our model predicts that absorption by the background gas is of minor importance. This is explained in more detail by the right-hand set of figures in Fig. 7, which show the number density profiles of Cu vapour (black continuous line) and background gas (grey continuous line), as well as the electron density profiles corresponding to the Cu vapour (black broken line) and background gas (grey broken line), for the different gases investigated, again at 8 ns. The Cu vapour density is clearly higher than the background gas density, and the same applies to the electron density originating from Cu vapour and

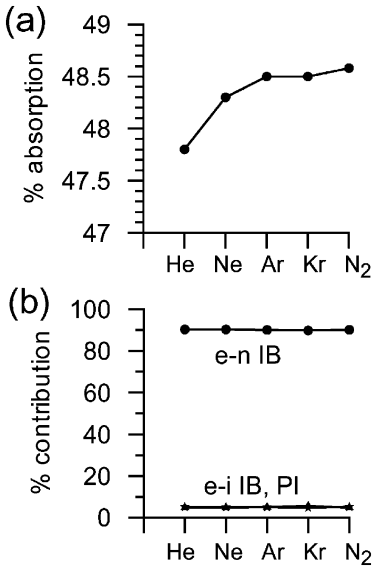

Fig. 8 Calculated relative amount of laser absorption in the plasma (a), and calculated relative contributions of electron–neutral and electron–ion inverse Bremsstrahlung (e–n IB and e–i IB) and photo-ionization (PI) as absorption mechanisms (b), for expansion in different gases, for the same laser conditions as in Fig. 1.

background gas. The latter is especially pronounced for the He background gas, because of the high ionization potential of He. The electron density originating from the background gas becomes non-negligible for the other gases, but even for Kr, which has the lowest ionization potential of the gases investigated, the electron density corresponding to the background gas is still significantly lower than the electron density corresponding to the Cu vapour. Hence, these figures explain why most of the laser absorption derives from the Cu vapor, as visualized in the left set of figures of Fig. 7.

Because the background gas has only a minor contribution to the plasma shielding, as predicted by our model, the calculated amount of plasma absorption is not greatly different for expansion in the different background gases, as is illustrated in Fig. 8(a). Indeed, the calculated amount of laser absorption increases from 47.8% for the case of He, to about 48.5% for expansion in Ar or Kr. The corresponding relative contributions of e–n IB, e–i IB and PI to the total amount of plasma shielding are depicted in Fig. 8(b). We calculated a relative contribution of roughly 90% for e–n IB, and of about 5% for both e–i IB and PI, for all gases investigated.

This relatively small effect of the background gas on the plasma shielding is a bit unexpected, in view of the statements made in the literature.[30–34] However, these statements are often based on secondary observations, such as the ICP emission intensities, which are integrated over several laser pulses, and where other effects can also play a role, such as more efficient vaporization of the particles (aerosol) in the ICP in the case of He gas, due to its higher thermal diffusivity. Moreover, experimental measurements in the plume itself, such as for the electron number density and plume temperature, are typically carried out at a much longer time after the laser pulse is finished, where the background gas will probably contribute to a larger extent to the plasma than in the early stage after laser ablation. Indeed, it was reported in ref. 39 that in the early stage of laser ablation, the ambient gas had no influence on the plume temperature, because the plasma is entirely composed of metal vapour, whereas after a few tens of ns, a mixed plasma begins to develop, and only after some hundreds of ns does the ambient gas reach the core of the metal plasma by diffusion. However, the plasma shielding is, of course, determined by the early stage, *i.e.*, during the laser pulse. On the other hand, it is also possible that the laser absorption mechanisms are not properly calculated in our model, because of rather large uncertainties in the absorption coefficients (see above). Moreover, in our model we consider only one laser pulse, and we disregard the possible influence of previous laser pulses, for instance vapour/gas mixing as well as gas plasma remaining from a previous laser pulse. Nevertheless, our calculated evaporation depths are in satisfactory agreement with measured crater depths (see above, Section 4.1), and these quantities are directly affected by the amount of plasma shielding, because it determines the laser intensity that can reach the target. Therefore, we expect that our model gives a realistic picture of the plasma shielding, and that the latter is indeed mainly determined by the Cu vapour, and not so much affected by the background gas.

4.4. Melting, evaporation and plasma formation thresholds in different background gases

Finally, we have investigated the effect of background gas on the thresholds for target melting and vaporization and for plasma formation, and the results are summarized in Fig. 9. We show only the results for expansion in He and Ar, because these gases are most frequently used, and the other background gases yield similar results, taking into account the effect of their ionization potential. We have only investigated the region between 0.1 and 1 GW cm^{-2}, because the thresholds for melting, vaporization and plasma formation are in this range. As appears from Fig. 9(a), the maximum surface temperature increases steadily with higher laser irradiance, and the background gas has nearly no effect, as was also observed in Fig. 1. The same applies to the maximum melting depth, plotted in Fig. 9(b). Melting starts to occur for a laser irradiance of about 0.1 GW cm^{-2}, for all gases investigated. Target evaporation starts at a somewhat higher laser irradiance of about 0.25 GW cm^{-2} (see Fig. 9(c)), but again, no distinct difference was found for expansion in the different background gases. However, at the higher laser irradiance values investigated, the calculated evaporation depth of Cu in the presence of He was found to be higher than in Ar, as a result of the higher amount of plasma shielding in Ar gas. It is expected that at still higher laser irradiance values, the influence of plasma shielding by the background gas will gradually become more important, because the ionization of the background gas will become more significant.

The effect of the background gas on the maximum plume temperature (Fig. 9(d)) and the maximum electron density (Fig. 9(g)) is found to be negligible in the early stage, as was also discussed above. Also, the calculated ionization degree of Cu vapour is very similar in the case of the different gases (*cf.* Fig. 9 (e) and (h)). Hence, the threshold for plasma formation

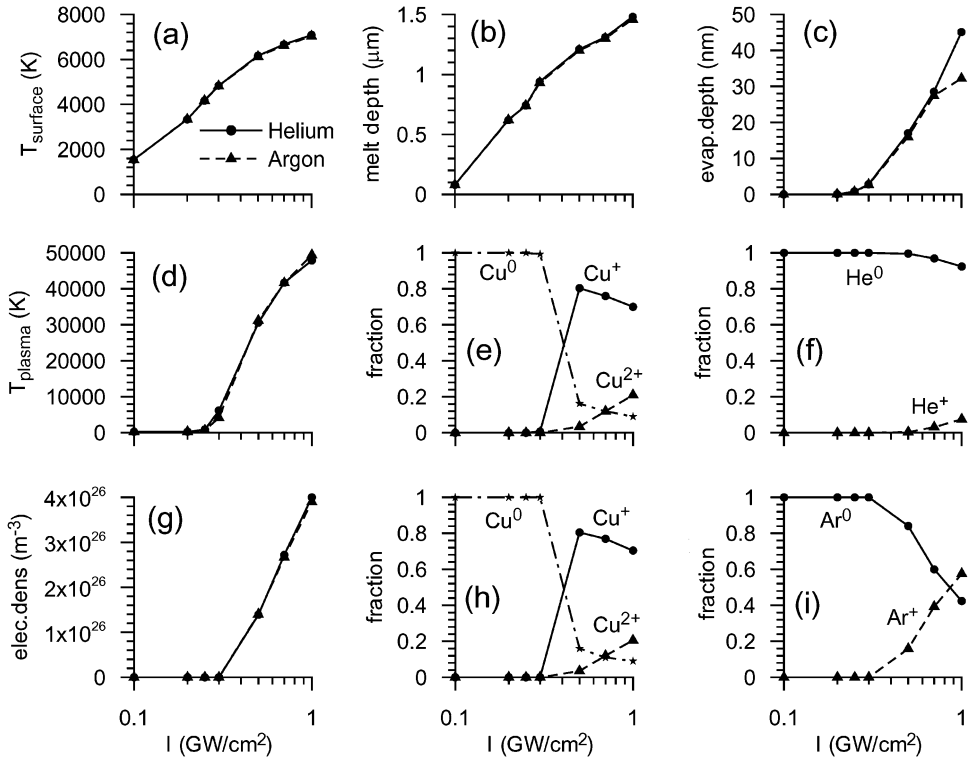

Fig. 9 Calculated maximum surface temperature (a), maximum melt depth (b), evaporation depth after 100 ns (c), maximum plume temperature at 8 ns (d), maximum electron density in the plasma at 8 ns (g), for expansion in He and Ar, and calculated fractions of Cu^0, Cu^+ and Cu^{2+} at 8 ns at the position of maximum plume temperature, for expansion in He (e) and Ar (h), and calculated fractions of He^0 and He^+ (f) and Ar^0 and Ar^+ (i) at 8 ns, at the position where the background gas contributes most to the electron density, as a function of laser irradiance. The other laser parameters are the same as in Fig. 1.

in the Cu vapour is predicted to be the same for expansion in the different background gases, and is slightly above 0.3 GW cm^{-2}. The calculated ionization degree of the background gas itself, on the other hand, is different for the different gases, due to the different values of the ionization potential. Figs. 9(f) and 9(i) show the ionization degrees of He and Ar, respectively, calculated at the position where the electron density corresponding to the background gas is at its maximum (*cf.* Fig. 7), *i.e.*, where the background gas gives the highest contribution to the electron density. In He, a plasma is formed only for a laser irradiance above 0.5 GW cm^{-2}, and even at 1 GW cm^{-2} the ionization degree of He is only less than 10%, whereas in the case of Ar, plasma formation starts for a laser irradiance above 0.3 GW cm^{-2}, and at 1 GW cm^{-2}, almost 60% of the Ar is calculated to be in ionized form. Note that these results were plotted for a time of 8 ns, hence at the maximum of the laser pulse. In summary, from this figure it can be concluded that the thresholds for target melting and vaporization and for plasma formation in the Cu plume are almost unaffected by the background gas used but, of course, the threshold for plasma formation in the background gas is determined by the ionization potential of the gas.

5. Conclusion

A comprehensive modeling network has recently been developed for laser ablation of metals, describing the laser-induced target heating, melting and vaporization, the subsequent vapour plume expansion in a background gas, the plasma formation in the plume, and the laser–plasma interaction. In the present paper, this model is applied to expansion in different background gases, *i.e.*, He, Ne, Ar, Kr and N_2.

It is observed that the heavier background gases, such as Ar and Kr, result in a slower expansion of the vapour plume, hence lower plume velocity and shorter plume length. The plume (or plasma) temperature and ionization degree of the metal vapour in the plasma seem not to be affected by the background gas, at least at the early stage of laser ablation (up to 100 ns). Also, the calculated electron density is very similar for expansion in the various background gases. Indeed, although the background gases with lower ionization potential exhibit a higher ionization degree in the plasma, their contribution to the total electron density is still of minor importance compared with the contribution of the metal vapour at the early stage of laser ablation. For the same reason, our model predicts that most of the laser–plasma interaction occurs with the metal vapour, so that plasma shielding is only a little bit more pronounced in the gases with lower ionization potential, such as Kr and Ar, than for instance in He. As a consequence, the target surface temperature was calculated to be very similar for the different background gases. Nevertheless, the small difference in the target surface temperature still yielded a non-negligible effect on the calculated target evaporation depths, which increase in the order Kr < Ar < Ne < He, whereas N_2 yielded very similar results to Ar. Further, our model predicts that the thresholds for target

melting (around 0.1 GW cm^{-2}) and vaporization (*ca.* 0.25 GW cm^{-2}) and for plasma formation in the Cu plume (slightly above 0.3 GW cm^{-2}) are almost unaffected by the background gas used, but the threshold for plasma formation in the background gas is, of course, determined by the ionization potential of the gas, and ranges from 0.3 to 0.5 GW cm^{-2}.

Finally, the calculated evaporation depths were compared with measured crater depths after a fixed number of laser pulses. After correcting for the number of laser pulses, and taking into account the different laser irradiance used in the experiments and the model calculations, the agreement between calculated and experimental results was found to be very reasonable, both with respect to the absolute values of the crater depths, and with respect to the influence of the different background gases. This suggests that our model presents a realistic picture of the laser ablation, evaporated plume expansion and plasma formation, and the laser–plasma interaction.

In summary, our calculation results show that the background gas has no significant effect on the ablation process and plasma shielding, in the early stage (first 100 ns), but that it does affect the plume expansion dynamics. Moreover, it will probably have a major influence on the transport of particles (aerosol) to the ICP and the subsequent vaporization in the ICP. Indeed, it is expected that He, as the lighter gas, will diffuse more quickly through the transport tube and thereby entrain the aerosol, compared with, for example, Ar. Moreover, He will more easily transfer heat to the aerosol, due to its higher thermal diffusivity, resulting in more efficient vaporization in the ICP and hence higher ICP signal intensities for solid sample introduction.

Acknowledgements

Z. Chen acknowledges financial support from a Bilateral Project between Flanders and China. D. Bleiner is financed by the Flemish Fund for Scientific Research. The authors thank A. Vertes for supplying the original code for laser ablation in vacuum, and A. Vertes and R. Gijbels for the interesting discussions. Finally, EMPA is acknowledged for the infrastructure of the experiments.

References

1 L. J. Radziemski, *Spectrochim. Acta, Part B*, 2002, **57**, 1109.
2 L. St.Onge, V. Detalle and M. Sabsabi, *Spectrochim. Acta, Part B*, 2002, **57**, 121.
3 J. D. Winefordner, I. B. Gornushkin, T. Correll, E. Gibb, B. W. Smith and N. Omenetto, *J. Anal. At. Spectrom.*, 2004, **19**, 1061.
4 J. M. Vadillo and J. J. Laserna, *Spectrochim. Acta, Part B*, 2004, **59**, 147.
5 D. Bleiner, *Spectrochim. Acta, Part B*, 2005, **60**, 49.
6 L. V. Zhigilei, *Appl. Phys. A*, 2003, **76**, 339.
7 A. B. Brailovsky, S. V. Gaponov and V. I. Luchin, *Appl. Phys. A*, 1995, **61**, 81.
8 J. H. Yoo, S. H. Jeong, R. Greif and R. E. Russo, *J. Appl. Phys.*, 2000, **88**, 1638.
9 Q. Lu, S. S. Mao, X. Mao and R. E. Russo, *Appl. Phys. Lett.*, 2002, **80**, 3072.
10 R. E. Russo, *Appl. Spectrosc.*, 1995, **49**, 14A.
11 D. Günther, S. E. Jackson and H. P. Longerich, *Spectrochim. Acta, Part B*, 1999, **54**, 381.
12 D. Günther, I. Horn and B. Hattendorf, *Fresenius' J. Anal. Chem.*, 2000, **368**, 4.
13 R. E. Russo, X. Mao and S. S. Mao, *Anal. Chem.*, 2002, **74**, 70A.
14 J. S. Becker, *Spectrochim. Acta, Part B*, 2002, **57**, 1805.
15 B. Hattendorf, C. Latkoczy and D. Günther, *Anal. Chem.*, 2003, **75**, 341A.
16 L. Balazs, R. Gijbels and A. Vertes, *Anal. Chem.*, 1991, **63**, 314.
17 A. Bogaerts, Z. Chen, R. Gijbels and A. Vertes, *Spectrochim. Acta, Part B*, 2003, **58**, 1867.
18 A. Bogaerts and Z. Chen, *J. Anal. At. Spectrom.*, 2004, **19**, 1169.
19 Z. Chen and A. Bogaerts, *J. Appl. Phys.*, 2005, **97**, 063305.
20 M. Aden, E. Beyer, G. Herziger and H. Kunze, *J. Phys. D: Appl. Phys.*, 1992, **25**, 57.
21 J. R. Ho, C. P. Grigoropoulos and J. A. C. Humphrey, *J. Appl. Phys.*, 1995, **78**, 4696.
22 A. Vertes, in *Laser Ablation: Mechanisms and Applications—II*, eds. J. C. Miller and D. B. Geohegan, AIP Conference Proceedings 288, AIP Press, New York, 1994.
23 M. Capitelli, F. Capitelli and A. Eletskii, *Spectrochim. Acta, Part B*, 2000, **55**, 559.
24 G. Callies, H. Schittenhelm, P. Berger and H. Hügel, *Appl. Surf. Sci.*, 1998, **127–129**, 134.
25 A. V. Gusarov, A. G. Gnedovets and I. Smurov, *J. Appl. Phys.*, 2000, **88**, 4352.
26 A. G. Gnedovets, A. V. Gusarov and I. Smurov, *J. Phys. D: Appl. Phys.*, 1999, **32**, 2162.
27 A. V. Gusarov, A. G. Gnedovets, I. Smurov and G. Flamant, *Appl. Surf. Sci.*, 2000, **154–155**, 331.
28 A. V. Gusarov and I. Smurov, *J. Phys. D: Appl. Phys.*, 2003, **36**, 2962.
29 A. Bogaerts and Z. Chen, *Spectrochim. Acta, Part B*, in the press.
30 X. L. Mao, O. V. Borisov and R. E. Russo, *Spectrochim. Acta, Part B*, 1998, **53**, 731.
31 A. P. K. Leung, W. T. Chan, X. L. Mao and R. E. Russo, *Anal. Chem.*, 1998, **70**, 4709.
32 W. T. Chan, A. P. K. Leung, X. L. Mao and R. E. Russo, *Appl. Surf. Sci.*, 1998, **127–129**, 269.
33 Y. Iida, *Spectrochim. Acta, Part B*, 1990, **45**, 1353.
34 W. Sdorra and K. Niemax, *Mikrochim. Acta*, 1992, **107**, 319.
35 S. L. Lui and N. H. Cheung, *Spectrochim. Acta, Part B*, 2003, **58**, 1613.
36 S. E. Jackson and D. Günther, *J. Anal. At. Spectrom.*, 2003, **18**, 205.
37 I. Horn, M. Guillong and D. Günther, *Appl. Surf. Sci.*, 2001, **182**, 91.
38 V. Detalle, M. Sabsabi, L. St.Onge, A. Hamel and R. Héon, *Appl. Opt.*, 2003, **42**, 5971.
39 A. Gomes, A. Aubreton, J. J. Gonzalez and S. Vacquié, *J. Phys. D: Appl. Phys.*, 2004, **37**, 689.
40 S. H. Jeong, R. Greif and R. E. Russo, *Appl. Surf. Sci.*, 1998, **127–129**, 1029.
41 H. Borchert, K. Darée and M. Hugenschmidt, *J. Phys. D: Appl. Phys.*, 2005, **38**, 300.
42 J. D. Anderson, *Computational Fluid Dynamics*, McGraw Hill, New York, 1995.
43 P. J. Shayler and M. T. C. Fang, *J. Phys. D: Appl. Phys.*, 1977, **10**, 1659.
44 S. Amoruso, R. Bruzzese, N. Spinelli and R. Velotta, *J. Phys. B*, 1999, **32**, R131.
45 J. G. Lunney and R. Jordan, *Appl. Surf. Sci.*, 1998, **127–129**, 941.